ON THE ORIGIN OF THE NEAR-INFRARED EMISSION FROM THE NEUTRON-STAR LOW-MASS X-RAY BINARY GX 9+1

The Astrophysical Journal, 834:71 (8pp), 2017 January 1 doi:10.3847/1538-4357/834/1/71

ON THE ORIGIN OF THE NEAR-INFRARED EMISSION FROM THE NEUTRON-STAR LOW-MASS X-RAY BINARY GX 9+1*

Maureen van den Berg[1,2] and Jeroen Homan[3,4]
[1] Harvard-Smithsonian Center for Astrophysics, 60 Garden Street, Cambridge, MA 02138, USA; maureen@head.cfa.harvard.edu
[2] Anton Pannekoek Institute for Astronomy, University of Amsterdam, Science Park 904, 1098 XH Amsterdam, The Netherlands
[3] Massachusetts Institute of Technology, Kavli Institute for Astrophysics and Space Research, 70 Vassar Street, Cambridge, MA 02139, USA
[4] SRON, Netherlands Institute for Space Research, Sorbonnelaan 2, 3584 CA Utrecht, The Netherlands
Received 2016 March 26; revised 2016 October 11; accepted 2016 October 14; published 2017 January 3

ABSTRACT

We have determined an improved position for the luminous persistent neutron-star low-mass X-ray binary and atoll source GX 9+1 from archival *Chandra X-ray Observatory* data. The new position significantly differs from a previously published *Chandra* position for this source. Based on the revised X-ray position we have identified a new near-infrared (NIR) counterpart to GX 9+1 in K_s-band images obtained with the PANIC and FourStar cameras on the *Magellan* Baade Telescope. NIR spectra of this $K_s = 16.5 \pm 0.1$ mag star, taken with the FIRE spectrograph on the Baade Telescope, show a strong Br γ emission line, which is a clear signature that we discovered the true NIR counterpart to GX 9+1. The mass donor in GX 9+1 cannot be a late-type giant, as such a star would be brighter than the estimated absolute K_s magnitude of the NIR counterpart. The slope of the dereddened NIR spectrum is poorly constrained due to uncertainties in the column density $N_{\rm H}$ and NIR extinction. Considering the source's distance and X-ray luminosity, we argue that $N_{\rm H}$ likely lies near the high end of the previously suggested range. If this is indeed the case, the NIR spectrum is consistent with thermal emission from a heated accretion disk, possibly with a contribution from the secondary. In this respect, GX 9+1 is similar to other bright atolls and the Z sources, whose NIR spectra do not show the slope that is expected for a dominant contribution from optically thin synchrotron emission from the inner regions of a jet.

Key words: accretion, accretion disks – binaries: close – stars: individual (GX 9+1) – X-rays: binaries

1. INTRODUCTION

Neutron-star low-mass X-ray binaries (NS-LMXBs) with weak magnetic fields show a wide variety in X-ray spectral and variability properties. Based on the correlated behavior of these properties, various NS-LMXB subclasses have been recognized; the atoll sources, the Sco-like Z sources, and the Cyg-like Z sources (Hasinger & van der Klis 1989; Kuulkers et al. 1994). Observations of the Z-source transient XTE J1701–462 have shown that these sub-classes are linked through mass accretion rate, with the atolls having the lowest mass accretion rates and the Cyg-like Z sources having the highest ones (Lin et al. 2009b; Homan et al. 2010). The differences in mass accretion rate between the sub-classes is likely the result of differences in system parameters, such as orbital period and properties of the donor star. However, for many NS-LMXBs these parameters are not well known, making it difficult to look for systematic differences in the system parameters between the NS-LMXB sub-classes.

The identification of an X-ray binary at optical or near-infrared (NIR) wavelengths is often a first step in gaining more insight into the binary parameters, the mass donor, or the accretion components (e.g., Casares et al. 1998; Harrison et al. 2014). Some LMXBs, however, remain unidentified in the optical or NIR due to a poorly determined X-ray position. One such source is GX 9+1, an NS-LMXB that has been persistently bright since its discovery in 1965 (Friedman et al. 1967). Together with GX 9+9, GX 3+1, Ser X-1, and 4U 1735–44, it forms a sub-group of atoll sources that spend most (or all) of their time in the spectrally soft state (Fridriksson 2011), also referred to as the "banana branch." Iaria et al. (2005) constrained the distance to GX 9+1 using an estimate of the neutral-hydrogen absorption column $N_{\rm H}$ toward the source, obtained from the modeling of *BeppoSAX* spectra. They derived a luminosity of $\sim 6 \times 10^{37}$ erg s^{-1} (0.12–18 keV) for a distance of 5 kpc, or $\sim$0.3 times the Eddington luminosity, $L_{\rm Edd}$. Despite the fact that the source has been known for more than half a century, we have hardly any information on its system parameters. Given that the absorption column toward GX 9+1 is substantial ($N_{\rm H} \approx 8 \times 10^{21}$ cm^{-2} at least; Iaria et al. 2005) a study of these parameters requires observations in the NIR band.

Several attempts to look for the optical or NIR counterpart of GX 9+1 around the *Einstein* X-ray position were undertaken, but remained unsuccessful (Hertz & Grindlay 1984; Gottwald et al. 1991; Naylor et al. 1991). In the most recent search by Curran et al. (2011), a tentative NIR counterpart was found based on the astrometric alignment of this star with a precise X-ray position obtained with the *Chandra X-ray Observatory*. However, all these studies, including the work by Curran et al., have in common that the search area for counterparts did not include the correct X-ray position. In this paper, we report the results of a new search for the NIR counterpart to GX 9+1 based on a revised *Chandra* position. In Section 2, we describe the observations and analysis of the X-ray and NIR data used in this paper. The new NIR counterpart is presented in Section 3. In the discussion of Section 4, we constrain the evolutionary status of the secondary, and consider the origin of the NIR emission in GX 9+1 in the context of the NIR properties of other luminous NS-LMXBs.

* This paper includes data gathered with the 6.5 m *Magellan* Telescopes located at Las Campanas Observatory, Chile.

Table 1
Chandra Observations of GX 9+1 Discussed in This Paper

ObsID	Detector	R.A.(J2000)	Decl.(J2000)	Uncertainty[a]	Remarks
717	ACIS-S/HETG	$18^h01^m32.26^s$	$-20°31'47.''9$	$0.''6$	Piled-up core
7030	HRC-I	$18^h01^m32.15^s$	$-20°31'45.''95$	$\leqslant 3''$	Large SIM offset
7031	ACIS-S	$18^h01^m32.23^s$	$-20°31'47.''83$	$0.''6$	Piled-up core
…	…	$18^h01^m32.15^s$	$-20°31'46.''1$	$0.''6$	Curran et al. (2011)

Note.
[a] 90% confidence radius on the absolute astrometry.

2. OBSERVATIONS AND DATA ANALYSIS

2.1. X-Rays

2.1.1. Chandra

GX 9+1 has been observed four times with *Chandra*. One of these observations (ObsID 6569) was done in continuous clocking mode and therefore does not provide useful imaging information. The properties of the remaining three observations are summarized in Table 1. The analysis of the observations was performed with CIAO 4.7. The observations were reprocessed using the `chandra_repro` script.

For the HRC-I observation (7030) we extracted an 800×800 pixel^2 image centered around GX 9+1, and ran the CIAO task `wavdetect` to obtain a source position. We note that during this observation the Science Instrument Module (SIM) was not in its usual position. Observations with a large SIM offset can have residual aspect offsets of up to $3''$, which is substantially larger than the typical error in the *Chandra* absolute astrometry of $0.''6$ (90% confidence) when the SIM is in its nominal position.[5] For this reason, we do not consider the position obtained from this observation very accurate. The position is listed in Table 1, and is a close match (only $0.''15$ different) to the *Chandra* position reported by Curran et al. (2011). These authors used a position that they obtained through private communication, and they did not provide any details of the *Chandra* analysis. Nevertheless, it is plausible that their adopted X-ray position is derived from ObsID 7030, and therefore, that their adopted positional uncertainty ($0.''6$) underestimates the actual uncertainty.

In the ACIS-S observation 7031 the image of GX 9+1 was heavily distorted due to a strongly piled-up core. While `wavdetect` cannot be used to obtain a source position in such a case, the deep and well-defined piled-up hole in the center of the source's image can still be used to obtain an accurate visual estimate of the source position. Since the observation was done with the nominal SIM offset, we assume a positional uncertainty of $0.''6$. The source position is listed in Table 1 and differs from the one obtained from observation 7030 by more than $2''$; the two positions are consistent, though, mainly due to the large error in the absolute astrometry of the latter.

Although the HETG was used during observation 717, the (zero-th order) image of GX 9+1 was still heavily distorted by pile-up. In this case we used the CIAO tool `tg_findzo`, which locates the position of the zero-th order centroid by finding the intersection of one of the grating arms with the detector readout streak. Like for observation 7031, we assume a positional uncertainty of $0.''6$. The position we obtain with this tool (see Table 1) is consistent with that obtained from observation 7031.

[5] http://cxc.harvard.edu/cal/ASPECT/celmon/

2.1.2. RXTE/ASM and MAXI Light Curves

We constructed a long-term light curve of GX 9+1 from publicly available *RXTE*/ASM (Levine et al. 1996) and *MAXI* (Matsuoka et al. 2009) data. For the *MAXI* data we used the 4.0–10.0 keV band, since the data in 2.0–4.0 keV band appeared to be affected by calibration issues after MJD ~56,200. To match the *MAXI* band as closely as possible, we used data in the 3.0–12.1 keV band for the ASM. Following van den Berg et al. (2014), we removed data points with large uncertainties ($\mathrm{ctr}/\sigma_{\mathrm{ctr}} < 20$, with σ_{ctr} the error on the count rate ctr). The count rates from both instruments were normalized to those of the Crab, in the selected energy bands. For *MAXI* we divided the count rates by an additional factor of 1.2, to match the count rates from the ASM around MJD 55,000–55,500. Finally, to reduce some of the scatter in the light curve, we rebinned the data in time by a factor of seven. The resulting light curve is shown in Figure 1. A strong long-term variation with a timescale of ~9.5 years is clearly visible. The short vertical lines in Figure 1 indicate the times of the NIR observations analyzed and/or discussed in this paper.

2.2. Magellan Near-infrared Observations

For this work we obtained NIR imaging and spectroscopy during four runs with the 6.5 m *Magellan* Baade Telescope in Las Campanas, Chile. Table 2 gives a summary of the runs, while more details of the observations and the data reduction are given below.

2.2.1. PANIC Imaging

We observed the field of GX 9+1 with the Persson's Auxiliary Nasmyth Infrared Camera (PANIC; Martini et al. 2004) on the nights of 2010 July 25 and 26. On the Baade Telescope, PANIC's 1024×1024 pixel^2 HgCdTe detector provides a $2' \times 2'$ field of view with a scale of $0.''127$ pixel^{-1}. The seeing improved from about $0.''9$ on the first night to $0.''55$ on the second night. On both nights, we obtained two consecutive K_s-band sequences of the GX 9+1 field. For each sequence we adopted a nine-point dither pattern, with three 10 s images taken at each dither position. Sky-background maps could not be constructed from the target exposures themselves as the field around GX 9+1 is too crowded. Instead, we obtained an exposure sequence of an interstellar dark cloud about $46'$ away, where the source density is much lower.

The PANIC package for IRAF was used to perform the basic data processing steps. These include dark-subtracting the

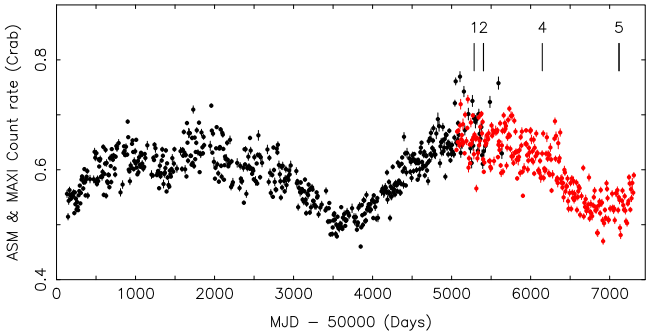

Figure 1. Long-term *RXTE*/ASM (black) and *MAXI* (red) light curves of GX 9+1. Each data point represents a ∼7 day average. The energy band used for the *RXTE*/ASM data is 3.0–12.1 keV, while that for the *MAXI* data is 4.0–10.0 keV. The short vertical lines indicate the epochs of our observations of the NIR counterpart to GX 9+1 as listed in Table 2; epoch 3 is not indicated as the star observed is not the true counterpart to GX 9+1.

Table 2
NIR Observations of the GX 9+1 Field Reported in This Paper

Epoch	Date (UTC)	MJD[a] (UTC)	Instrument	$T_{\rm exp}$ (s)	Seeing ($''$)
1[b]	2010 Mar 29	55284.40076	SOFI	540	1.4
2-a	2010 Jul 25	55402.05384	PANIC	540	0.9
2-b	2010 Jul 26	55403.00737	PANIC	540	0.55
3	2012 May 1	56048.36185	FIRE	3614	0.45
4	2012 Aug 8	56146.97466	Fourstar	707	0.9
5-a	2015 Apr 5	57117.35880	FIRE	4217	0.4
5-b	2015 Apr 6	57118.36038	FIRE	4819	0.4

Notes.
[a] Modified Julian Date at the midpoint of the observation.
[b] Data retrieved from the ESO archive. More details can be found in Curran et al. (2011).

science exposures, averaging the frames taken at each dither position, correcting for nonlinearity of the detector response, applying a flat-field correction using master twilight flats, and correcting for the astrometric distortion. The processed frames of the offset field were median-combined to create an initial sky map. After masking out any objects detected in the sky-subtracted offset images, the median combining was repeated to make the final sky map. The sky-subtracted target frames were then aligned and stacked into one master K_s image for each night. The astrometry of the stacked images was tied to the International Celestial Reference System (ICRS) using the Two Micron All Sky Survey (2MASS) catalog (Skrutskie et al. 2006). We fitted the measured positions of ∼45 unsaturated and relatively isolated stars to their 2MASS positions, solving for zero point, rotation angle, and scale factor. The adopted fits have an rms scatter of ∼0.″06 in right ascension and declination, which is comparable to the errors in the absolute astrometry of the 2MASS catalog. We used point-spread-function (PSF) fitting photometry to extract magnitudes for stars in the field. For each night separately, the photometric calibration was derived by computing the average difference between the instrumental magnitudes of twelve isolated stars and the K_s magnitudes of their 2MASS counterparts. We adopt the rms scatter around the mean offset as the error in the photometric calibration, which amounts to 0.088 mag for both nights.

2.2.2. FourStar Imaging

On 2012 August 8 we re-observed the field of GX 9+1 with the FourStar camera (Monson et al. 2011) on the Baade Telescope under a seeing of ∼0.″9. The 2 × 2 array of four 2048 × 2048 pixel^2 HAWAII-2RG detectors images a 10.′8 × 10.′8 field with a 0.″159 pixel^{-1} scale; GX 9+1 was centered on one of the detectors. We obtained a sequence of K_s-band exposures arranged in a nine-point dither pattern, with nine exposures of ∼8.7 s taken at each dither position for a total exposure time of 707 s. The same sequence was executed on a pointing to a relatively empty offset field to obtain the observations needed for constructing a sky background map.

We adopted a data-reduction procedure similar to the one described in Section 2.2.1, except that we used the `SCAMP` package (Bertin 2006) to map out the variable pixel scale over the chip area based on the measured positions of 2MASS stars in the field. The distortion correction was applied and the stacked K_s image was resampled to a linear pixel scale of 0.″12 pixel^{-1} (similar to the PANIC pixel scale) with the `SWarp` routines (Bertin et al. 2002). The small degree of oversampling compared to the native FourStar pixel scale is justified by the non-integer offsets of the dither sequences. We tied the astrometry to the ICRS in the same way as we did for the PANIC images, which resulted in an astrometric solution with an rms scatter of 0.″052 in right ascension and 0.″073 in declination based on a fit to the positions of 36 2MASS stars. Magnitudes were calibrated to 2MASS with an rms scatter of 0.050 mag using thirteen relatively isolated stars.

2.2.3. FIRE Spectroscopy

We used the Folded-port InfraRed Echellette (FIRE; Simcoe et al. 2013) spectrograph on the Baade Telescope to observe two objects. The NIR counterpart proposed by Curran et al. (2011), which we designate star A, was observed during a run on 2012 May 1. After we revised the X-ray position of GX 9+1 based on *Chandra* ObsIDs 717 and 7031, we observed the new candidate counterpart, called star B hereafter, during a run on 2015 April 5 and 6. More details on the properties of these stars are given in Section 3. For star A we obtained six 602-s exposures when the object was at an airmass of ∼1. Star B was observed at an airmass of 1–1.1, for a total of eighteen 602-s exposures. The adopted instrument rotation angle was such that the nearest neighbors to the target did not fall in the slit. Seeing conditions during both runs were excellent ($\lesssim$0.″45). On both occasions we used FIRE in echelle mode with a slit width of 0.″6, which yields spectra with a continuous wavelength coverage of 0.82–2.51 μm spread over 21 orders at a resolving power of $R \approx 6000$. The HAWAII-2RG detector provides a pixel scale in the spatial direction of 0.″18 pixel^{-1}. Target observations were bracketed with observations of bright telluric standards of spectral type A0 V.

Data reduction and the spectral extraction were done with FIREHOSE, the custom-developed data processing pipeline for FIRE (Bochanski et al. 2011). The wavelength calibration was done using ThAr lamp exposures taken immediately before or after the target exposures, and OH sky emission lines in the target exposures themselves. The typical errors in the dispersion solution are $\lesssim$0.3 Å. Redward of 2.3 μm the wavelength calibration is more uncertain because very few useful calibration lines are present. Spectra of the NS-LMXB GX 1+4 (Chakrabarty & Roche 1997) and the likely white-

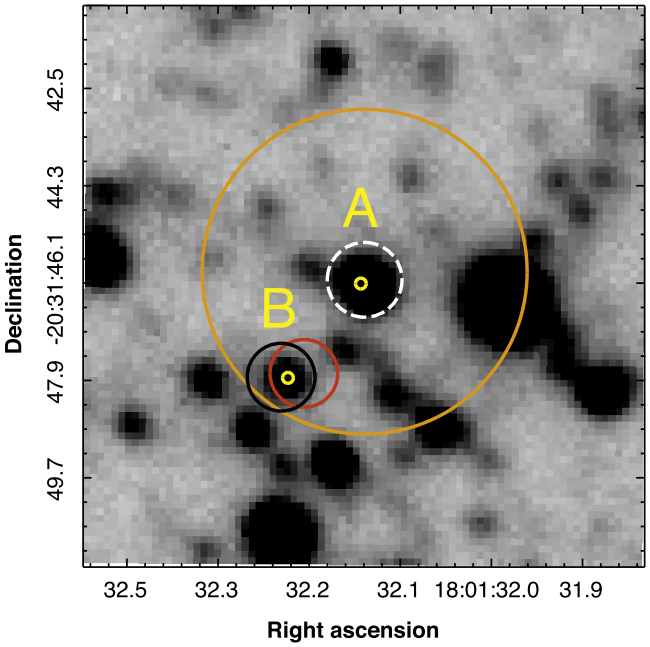

Figure 2. PANIC K_s-band image of the region around GX 9+1 from 2010 July 26. Stars A and B are marked with small yellow circles. The *Chandra* positions from ObsIDs 717, 7030, and 7031 are at the center of the black, orange, and red circles, respectively, which have radii equal to the combined X-ray/NIR 90% confidence errors on the position, r_{90}. For ObsIDs 717 and 7031 $r_{90} = 0\farcs63$, and for ObsID 7030 $r_{90} = 3''$. The position and error radius adopted by Curran et al. (2011) are represented by the dashed white circle with $r_{90} = 0\farcs69$. The image is $10'' \times 10''$; north is up, east is to the left.

dwarf symbiotic binary BW 3 (van den Berg et al. 2006), which are both accreting binaries with an M-giant secondary, were obtained during the 2015 FIRE run immediately following the target observations. The prominent CO absorption bands from the donor star that are present in the spectra of both objects, can be used to check the wavelength calibration beyond 2.3 μm. Correction for telluric absorption was accomplished with the method and routines described in Vacca et al. (2003) as implemented in FIREHOSE.

3. RESULTS

The *Chandra* positions for GX 9+1 from Table 1 are marked on our PANIC image from 2010 July 26 in Figure 2. The error circles shown represent the respective 90% confidence radii on the source positions (r_{90}), in which the absolute pointing error on the X-ray position (column 5 in Table 1) and the error on the NIR astrometry are combined in quadrature. The 1σ error on the NIR astrometry is $0\farcs084$ for our PANIC image, and $0\farcs16$ for the astrometry of Curran et al. (2011); before combining these errors with the X-ray astrometric error, both are scaled to a 90% confidence radius assuming a 2D Gaussian distribution. Star A lies only $\sim 0\farcs23$ from the X-ray position that follows from ObsID 7030, and only $\sim 0\farcs1$ from the Curran et al. position. Given the close proximity to their adopted X-ray position and the lack of other stars in their adopted error circle, Curran et al. considered A the likely counterpart to GX 9+1. However, they assumed an uncertainty on the X-ray position that is much smaller than the up to $3''$ that is warranted by the large SIM offset. Star A is in fact only one of about a dozen candidate NIR counterparts inside the actual 90% error circle around their adopted X-ray position. On the other hand, the more accurate position derived from *Chandra* ObsIDs 717 and 7031 is only consistent with one NIR source that we detected, viz. star B. The positions and K_s photometry of both stars are reported in Table 3.

Our FIRE spectra of the two stars indeed show that B is the counterpart of GX 9+1. Its spectrum shows the Brackett (Br) γ line at 2.166 μm in emission—a signature that is commonly seen in the NIR spectra of LMXBs (e.g., Bandyopadhyay et al. 1997, 1999). In the stacked spectra of both nights of run 5, this emission feature is broad and has an equivalent width (EW) of about -7 ± 2 Å. No other significant emission or absorption lines can be seen but we note that above $\sim$2.34 μm the spectrum is very noisy. The spectrum of star A, on the other hand, shows numerous absorption features that can be identified with atomic lines and molecular bands present in the NIR spectra of late-type stars (Rayner et al. 2009). The clear ^{12}CO absorption features between $\sim$2.29 and 2.39 μm, and the comparatively weak absorption lines of the Brackett series, constrain the spectral type of A to be somewhere between late-G and early-K. Figure 3 shows the spectra of both objects around Br γ. Below $\sim$1 μm the spectra have a low signal-to-noise, a sign that both stars are significantly reddened.

The shape of the Br γ line of star B looks asymmetric, with the part lying to the red of the emission peak having a steeper slope than the blue side. The widths that correspond to the blue and red side, respectively, are about -1000 km s^{-1} and 500 km s^{-1}, where we define the width as the approximate separation between the wavelength of the peak flux and the wavelength where the flux reaches the continuum (either on the blue or red side). This asymmetry is visible in the stacked spectra of both nights. Higher signal-to-noise, or higher resolution, spectra are needed to further investigate this asymmetry, which could be a signature of multiple emission components in the system centered at different velocities.

With our very limited temporal sampling, we can say little about brightness variations of star B. In order to complement our own photometry, we analyzed the K_s images of the GX 9+1 field presented in Curran et al. (2011). The data set consists of nine dithered images taken on 2010 March 29 with the Son OF ISAAC (SOFI) infrared spectrograph and camera on the 3.6 m ESO New Technology Telescope (NTT) at La Silla, Chile. The total exposure time is 540 s. After applying the SOFI data-reduction steps as outlined in the SOFI manual[6] (linearity and crosstalk correction, flatfielding, sky subtraction), we combined these images into a single stacked image. The astrometry and photometry were calibrated against 2MASS in a similar way as described in Sections 2.2.1 and 2.2.2. Due to the poor seeing ($1\farcs4$) and coarser pixel scale of SOFI ($0\farcs288$ pixel^{-1}), star B is blended with at least two neighbors; we find $K_s = 16.10 \pm 0.08$ for the blend.

We also searched the source catalog of the UKIDSS Galactic Plane Survey (GPS; Lucas et al. 2008) for any detections of star B, but found no entries for this star in the latest publicly available GPS catalog (UKIDSSDR8plus). In the co-added interleaved *JHK* images of the GPS, star B appears blended with its neighbor to the southeast. Finally, we checked if star B is included in the catalogs of the VISTA Variables in the Via Lactea (VVV) Survey (Minniti et al. 2010). Star B appears neither in the single-epoch, filter-merged ($ZYJHK_s$) source catalog, nor in the variable-star catalog of VVV Data Release 2 (DR2). However, in the single-filter catalogs that are associated

[6] https://www.eso.org/sci/facilities/lasilla/instruments/sofi/doc/manual/sofiman_2p30.pdf

Table 3
NIR Astrometry and Photometry for Stars A and B

ID	R.A. (J2000)[a]	Decl. (J2000)	Δ[b] (″)	Epoch 1	Epoch 2-a	Epoch 2-b	Epoch 4	VVV[c]
A	$18^h01^m32.155^s$	−20° 31′46.″17	2.27	$K_s = 15.09(2)$	$K_s = 15.06(1)$	$K_s = 15.05(1)$	$K_s = 15.06(1)$	$K_s = 15.00(5)$, $H = 15.41(5)$, $J = 16.76(5)$
B = GX 9+1	$18^h01^m32.251^s$	−20° 31′47.″91	0.13	$K_s > 16.1$	$K_s = 16.48(1)$	$K_s = 16.43(1)$	$K_s = 16.53(1)$	$K_s = 16.3(1)$[d], $J = 17.8(1)$[d]

Notes.
Numbers in parentheses are the errors in the last significant digit and are the DAOPHOT errors on the PSF photometry. Additional errors in the photometric calibration with respect to 2MASS are 0.05 mag for Epoch 1, 0.09 mag for Epochs 2-a and 2-b, and 0.05 mag for Epoch 4.
[a] Positions derived from the PANIC image of 2010 July 26.
[b] Angular offset between the NIR positions and the *Chandra* position derived from ObsID 7031.
[c] VVV magnitudes were converted to the 2MASS system using equations on http://casu.ast.cam.ac.uk/surveys-projects/vista/.
[d] Object could be blended.

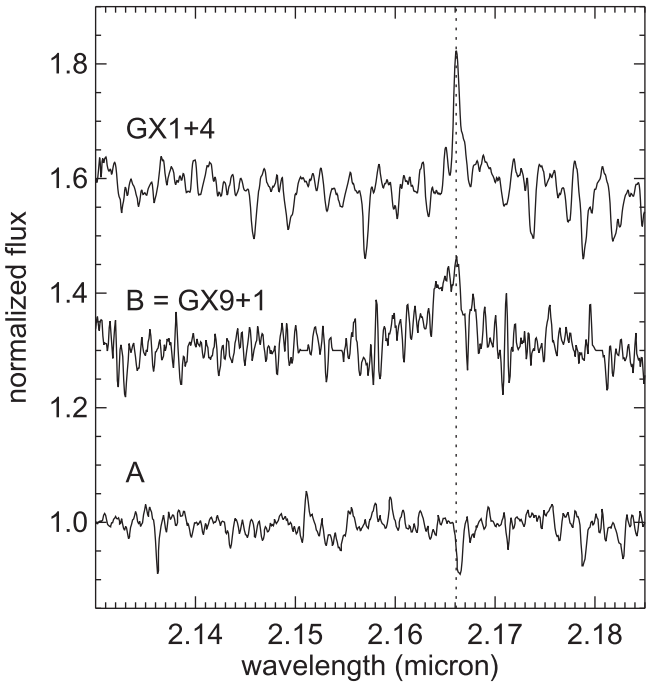

Figure 3. The continuum-normalized FIRE spectrum of star B (GX 9+1; middle) shows an emission line at 2.166 μm (dotted line) that can be identified with Br γ; this clearly demonstrates it is the counterpart to GX 9+1. The spectrum of A (bottom) shows a weak Br γ absorption line. For comparison, we also include the spectrum of the NS-LMXB GX 1+4 (top), which also has Brγ in emission; this spectrum was corrected for the systemic radial velocity of GX 1+4 (Hinkle et al. 2006). Arbitrary offsets of +0.3 and +0.6 have been applied to the fluxes of B and GX 1+4, respectively. The spectra of A and B have been smoothed with a bin size of 3 pixels to suppress the noise. The fluxes in three narrow regions in the spectrum of B that were impacted by non-optimal sky-subtraction have been set to 1.

with the 61 VVV DR4 images that include the region around GX 9+1, we find two detections of star B: $J = 17.8 \pm 0.1$ (from an observation on 2010 April 12) and $K_s = 16.3 \pm 0.1$ (from 2012 July 22). Since in both cases the detections are flagged as "non-stellar" (likely because of blending with the neighbor), these magnitudes should be regarded with caution.

We note that star A is detected in the VVV DR2 catalog (see Table 3) and the UKIDSS GPS catalog (with $J = 16.84(4)$, $H = 15.60(3)$, and $K_s = 15.07(3)$ in the 2MASS system; calibration from Lucas et al. 2008). From the SOFI images we derive $K_s = 15.09 \pm 0.06$ for A. This is consistent with the PANIC, GPS, and VVV values, but significantly different than the value quoted in Curran et al. (2011), viz. $K_s = 15.35 \pm 0.04$, even though the two measurements are derived from the same data.

4. DISCUSSION

Having identified the NIR counterpart to GX 9+1, we can now explore the nature of the mass donor and the origin of the NIR emission. In order to derive the intrinsic spectral shape of the NIR emission, it is necessary to first review the column density N_H and (optical or NIR) extinction A toward GX 9+1, and, connected to those factors, its distance d (Section 4.1). The suggested ranges in N_H, A, and d have little impact on our conclusions regarding the donor (Section 4.2). On the other hand, N_H and A do affect the slope of the dereddened NIR spectrum—and therefore the interpretation of its origins—quite significantly (Section 4.3). Based on the implications of the choice of N_H for the distance and X-ray luminosity of GX 9+1, we argue below in Section 4.1 that a value of N_H near the high end of the suggested range is more likely.

4.1. Column Density and Distance

The estimate of $d = 5$ kpc that was adopted by Iaria et al. (2005) was chosen to lie in between the values that follow from two extremes in N_H. In their best-fitting model to the GX 9+1 *BeppoSAX* spectra, N_H is as low as $(8 \pm 1) \times 10^{21}$ cm^{-2}. Using the Taylor & Cordes (1993) model for the spatial distribution of the ionized hydrogen in the Galaxy, combined with an assumed ionized-hydrogen fraction of 10%, Iaria et al. estimated that the corresponding distance is 4.4 ± 1.3 kpc. Alternative modeling of the *BeppoSAX* spectra at especially the lower energies, resulted in an N_H that is almost two times higher. A higher column density was also reported by others; White et al. (1988) derived $N_H \approx 1.5 \times 10^{22}$ cm^{-2} or even higher, and more recently, Valencic & Smith (2015) found $N_H = 1.24(5) \times 10^{22}$ cm^{-2}. The distance estimate increases accordingly, to about 6.4 ± 1.9 kpc for $N_H = 1.5 \times 10^{22}$ cm^{-2} in the Taylor & Cordes model (Iaria et al. 2005).

Using more recent maps of the Galactic extinction to turn N_H into a distance, we find relatively small distances for the lower limit of $N_H = (8 \pm 1) \times 10^{21}$ cm^{-2}, viz. 3.7 ± 0.3 kpc (based

on the Drimmel et al. 2003 map for the optical extinction A_V), and 2.1 ± 0.3 kpc (for the Schultheis et al. 2014 $E(J-K_s)$ maps[7]). We used Nishiyama et al. (2008, 2009) to convert the NIR extinction to the V-band extinction ($A_V : A_J : A_{K_s} = 1 : 0.188 : 0.062$), and $N_{\rm H} = 1.79(3) \times 10^{21}\ A_V\ {\rm cm}^{-2}$ (Predehl & Schmitt 1995). Valencic & Smith (2015) and Güver & Özel (2009) derived higher $N_{\rm H}/A_V$ ratios, viz. $N_{\rm H} = 2.08(9) \times 10^{21}\ A_V\ {\rm cm}^{-2}$ and $N_{\rm H} = 2.21(9) \times 10^{21}\ A_V\ {\rm cm}^{-2}$, respectively. The distance to GX 9+1 based on these relations, is even smaller: using Güver & Özel (2009), we find values down to 3.3 ± 0.3 kpc (Drimmel) and 1.7 ± 0.2 kpc (Schultheis). These estimates place GX 9+1 in front, or at most on the near edge, of the Galactic bulge. However, the concentration of many bright X-ray binaries—including GX 9+1—in the direction of the bulge, makes it plausible that many are actually located *in* the bulge. This implies a conservative lower limit of $d \approx 4$ kpc according to the Galaxy model by Picaud & Robin (2004). This consideration does not put a firm constraint on the distance to any individual X-ray binary, but it does make these small distances for GX 9+1, and therefore low column densities, less likely.

Another argument against a small distance comes from comparing the X-ray properties of GX 9+1 with those of the transient NS-LMXB XTE J1701–462. This system has a distance estimate (8.8 ± 1.3 kpc, Lin et al. 2009a) obtained from two type I radius expansion bursts. During the decay of its 2006/2007 outburst it displayed X-ray behavior quite similar to GX 9+1, i.e., it traced out tracks in its color–color (CDs) and hardness-intensity diagrams (HIDs) that have shapes similar to those of GX 9+1. The closest resemblance between the CD/HID tracks of GX 9+1 (Fridriksson 2011) and XTE J1701–462 (Lin et al. 2009b; Homan et al. 2010) occurs for a bolometric luminosity range of the latter of about (6–18) × 10^{37} erg s^{-1} (see Figures 3 and 5 in Lin et al. 2009b). Given the 0.12–18 keV flux reported by Iaria et al. (2005) (∼2.0 × 10^{-8} erg cm^{-2} s^{-1}), a distance of $\lesssim$4 kpc would imply a luminosity of $\lesssim$3.8 × 10^{37} erg s^{-1} for GX 9+1. Such low values are at odds with the luminosity suggested by the analogy with XTE J1701–462.[8]

An $N_{\rm H}$ of 1.5 × 10^{22} cm^{-2} gives a distance of ∼7 kpc (Drimmel) or 5.5 kpc (Schultheis) when using Predehl & Schmitt (1995), or 4.9 kpc (Drimmel) or 3.3 kpc (Schultheis) when using Güver & Özel (2009). Except for the latter estimate, this is more in line with a bulge origin of GX 9+1.

4.2. Constraints on the Nature of the Secondary in GX 9+1

High mass accretion rates (∼10^{-9}–10^{-8} $M_\odot$ yr^{-1}) are required to power the most luminous NS-LMXBs, which are thought to be accreting up to ∼0.5 $L_{\rm edd}$ (for the bright atolls) or even close to or above the Eddington limit (Z sources). It has been suggested that the mass donors in these systems are evolved stars, whose evolutionary expansion upon ascent of the giant branch drives the high mass transfer rate (Taam 1983; Webbink et al. 1983). For the persistent Z sources with known orbital periods (P_b) this is indeed a plausible scenario: Sco X-1, Sco X-2, Cyg X-2, and GX 13+1 have orbital periods between ∼19 hr and ∼25 day (Gottlieb et al. 1975; Cowley et al. 1979; Wachter & Margon 1996; Iaria et al. 2014), which is too long for a Roche–lobe-filling main-sequence star. On the other hand, the (tentative) orbital periods of the bright atolls Ser X-1 (∼2 hr; Cornelisse et al. 2013), GX 9+9 (4.2 hr; Hertz & Wood 1988), and 4U 1735–44 (4.7 hr; Corbet et al. 1986) are in the expected range for a main-sequence donor. Similarly, the estimated absolute K_s magnitudes (M_{K_s}) of the NIR counterparts to GX 3+1 and 4U 1705–44 (a source that is often as bright as the other bright atolls) exclude that the neutron star is fed by a late-type giant (van den Berg et al. 2014; Homan et al. 2009). This implies that other scenarios must be invoked to explain the high accretion rate in these systems (see e.g., Verbunt & Zwaan 1981), although the distinction in orbital period between Z sources and bright atolls cannot be that straightforward. With $P_b \approx 21$ hr (Jones & Watson 1989), the luminous dipping atoll source 4U 1624–49 likely hosts an evolved star. Conversely, with an estimated $M_K \approx +2.9$ (Jonker et al. 2000) in the non-flaring state, the Z-source GX 17+2 is far too faint to allow a giant donor if the assumed distance of ∼7.5 kpc is correct (see also Callanan et al. 2002).

Evidently, the distance to GX 9+1 is poorly determined as a result of uncertainties in $N_{\rm H}$, the Galactic distribution of the absorbing material, and the relation between $N_{\rm H}$ and A_V. However, none of the combinations for $N_{\rm H}$, A_V, and d described above predict an absolute K_s magnitude of GX 9+1 that is less than $M_{K_s} = 1.4$. For example, for $d = 4$ kpc (the minimum plausible distance) and $N_{\rm H} = 8 \times 10^{21}$ cm^{-2}, $M_{K_s} \approx 3.3$, while for $d = 8.3$ kpc (the maximum distance according to the Taylor & Cordes model) and $N_{\rm H} = 1.5 \times 10^{22}$ cm^{-2}, $M_{K_s} \approx 1.4$ (the choice of $N_{\rm H}/A_V$ ratio has an effect of $\lesssim$0.1 mag). Like in most bright atolls, a giant secondary for GX 9+1 is therefore excluded, as giants with spectral types of G0 or later have $M_{K_s} \lesssim -0.45$ (Bessell & Brett 1988; Ostlie & Carroll 2007) and are therefore brighter than GX 9+1 in the K_s band. Main-sequence secondaries of spectral type G0 to M5 have $M_{K_s} = 3.0$–8.4.[9] In the K_s band, an M5 dwarf would therefore contribute only ∼1% of the light at most, if GX 9+1 would have $M_{K_s} \approx 3.3$. As a result, there is no hope of detecting its Na I absorption lines at 2.206 μm and 2.209 μm or its ^{12}CO bandhead at 2.294 μm (the strongest features in this wavelength range; Rayner et al. 2009) in our spectra, which have a signal-to-noise ratio $S/N \approx 25$ around 2.1–2.2 μm, and $S/N \approx 5$ around 2.29 μm. Even a G0 or K0 dwarf would be difficult to detect: their strongest absorption features in the K_s band (apart from Br γ) have a depth of at most ∼10% below the continuum, so even if such a star would dominate the K_s-band emission, the depth of these lines would at most be similar to the 3σ noise level. Our non-detection of any spectral features other than the Br γ emission line is therefore consistent with the secondary being a late-type dwarf.

4.3. The Origin of the NIR Emission in GX 9+1

Synchrotron emission and thermal emission can both contribute to the NIR spectra of luminous NS-LMXB binaries. The dominant emission process can be inferred from the spectral slope, i.e., the index α if the spectra are written as $F_\nu \propto \nu^\alpha$ with F the flux and ν the frequency.

[7] Schultheis et al. (2014) compute maps of $E(J-K_s)$ versus distance and of $E(H-K_s)$ versus distance, but for simplicity we only report the results for the former here. The $E(H-K_s)$ maps predict distances that are about 15% smaller.

[8] Here we have assumed that 0.12–18 keV luminosity is close to the bolometric value.

[9] http://www.pas.rochester.edu/~emamajek/EEM_dwarf_UBVIJHK_colors_Teff.txt

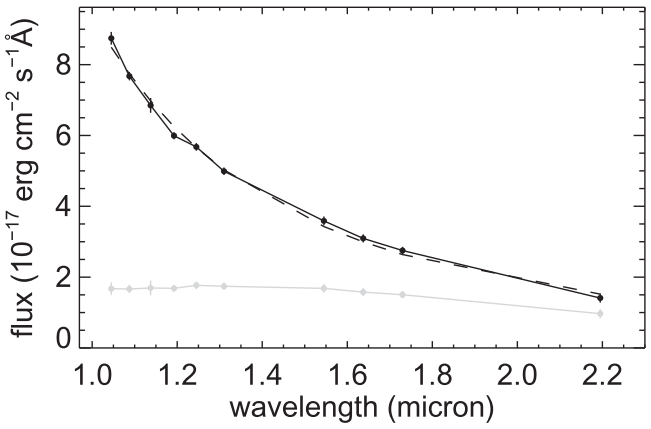

Figure 4. Observed (gray) and dereddened (black) spectral energy distributions of GX 9+1. For each echelle order of the FIRE spectrum that is not significantly contaminated by atmospheric absorption, the average flux is plotted and the error bar represents the standard deviation of the flux. The spectrum that is shown here was dereddened assuming $N_{\rm H} = 15 \times 10^{21}$ cm^{-2}, $N_{\rm H}/A_V = 2.21 \times 10^{21}$ (Güver & Özel 2009), and the Nishiyama et al. (2009) extinction law ($A_\lambda \propto \lambda^{-2.0}$). Overplotted with a dotted line is a function of the form $F_\lambda \propto \lambda^{-2-\alpha}$ with $\alpha = 0.32 \pm 0.15$ (see discussion in Section 4.3).

In systems where accreted matter is carried away from the system via a jet, synchrotron emission from the jet is detected in the radio and, in some cases, all the way to the NIR/optical. The signature characteristic of the optically thick part of a steady jet is the flat-spectrum ($\alpha \approx 0$) radio emission. Emission from the optically thin inner regions of the jet can be significant at higher frequencies, and produces a distinctive negative spectral index ($\alpha < 0$). For example, millisecond X-ray pulsars and atolls that are less luminous than GX 9+1 but have $L_{\rm X} \gtrsim 10^{36}$ erg s^{-1} (Russell et al. 2007) display such red NIR spectra. For most NS-LMXBs it is unclear at which frequency the break between optically thick and thin synchrotron emission occurs. In 1RXS J180408.9–342058, the outburst NIR/optical emission at frequencies as high as the SDSS r band showed a flat spectrum when the source was in an X-ray hard state (Baglio et al. 2016). For 4U 0614+091 the break lies in the mid-IR (Migliari et al. 2010), with the optically thin component declining toward the NIR, at which point it is dominated by thermal emission.

In cases like 4U 0614+091, or when a jet is absent to begin with, thermal emission from an X-ray-heated or viscously heated accretion disk, or from the (possibly X-ray-heated) secondary, gives rise to a positive α. Specifically, emission dominated by X-ray reprocessing results in $0.5 \lesssim \alpha \lesssim 2$, whereas for a viscously heated disk the expected α is 1/3 or 2 (Frank et al. 1992; Hynes 2005; Russell et al. 2007). With the exception of GX 17+2 (Harrison et al. 2011), thermal emission typically dominates the NIR spectra of the Z sources (Russell et al. 2007; Harrison et al. 2014), all of which have been detected as radio-jet sources[10] (Fender & Hendry 2000). Emission from an irradiated disk can also explain the NIR spectrum of the two luminous atolls 4U 1705-44 and GX 3+1 (Homan et al. 2009; van den Berg et al. 2014), for which a radio jet has never been detected.

[10] Another manifestation of optically thin synchrotron emission is linear polarization of the light. This has been observed, for example, in Sco X-1 and Cyg X-2 (e.g., Shahbaz et al. 2008). These systems have $\alpha_{\rm NIR} > 0$ but, based on the observed polarization, the synchrotron component is not altogether absent from the NIR.

Table 4
Results for the NIR Spectral Index α

$N_{\rm H}$ (cm^{-2})	A_V	α (N09)	α (CCM89)
8×10^{21}	4.5 (PS)	-0.40 ± 0.12	-0.08 ± 0.13
	3.6 (GO)	-0.65 ± 0.12	-0.38 ± 0.12
1.5×10^{22}	8.4 (PS)	0.87 ± 0.16	1.56 ± 0.18
	6.8 (GO)	0.32 ± 0.15	0.9 ± 0.1

Note.
Summary of the values of the spectral index α that result from fits to the FIRE spectrum of GX 9+1. The spectrum was dereddened using different assumptions about $N_{\rm H}$, $N_{\rm H}/A_V$ (PS—Predehl & Schmitt 1995, GO—Güver & Özel 2009), and the NIR extinction law (N09—Nishiyama et al. 2009, CCM89—Cardelli et al. 1989).

To uncover the origin of the NIR emission in GX 9+1, we have fitted the dereddened FIRE spectrum with a power-law shape (see Figure 4). Taking the suggested range in $N_{\rm H}$ at face value, we find that the spectral index is poorly constrained; the possible range in $N_{\rm H}/A_V$ ratios only makes it worse. Fits to the spectrum that is dereddened using the Nishiyama et al. (2009) extinction law, give $\alpha \approx -0.40 \pm 0.12$ for $N_{\rm H} = 8 \times 10^{21}$ cm^{-2}, and $\alpha \approx 0.87 \pm 0.16$ for $N_{\rm H} = 1.5 \times 10^{22}$ cm^{-2} for the Predehl & Schmitt (1995) $N_{\rm H}/A_V$ ratio.[11] For the Güver & Özel (2009) ratio, the spectral index is smaller, viz. $\alpha \approx -0.65 \pm 0.12$ and $\alpha \approx 0.32 \pm 0.15$ for the low and high $N_{\rm H}$ value, respectively. The Nishiyama NIR extinction law is appropriate toward the Galactic center. Since GX 9+1 is located about 10° away from this direction, we have also considered the Cardelli et al. (1989) extinction law. The effect is to increase the values of α (see the last column in Table 4).

As discussed in Section 4.1, we consider the lower $N_{\rm H}$ values less likely as they imply a rather small distance and low X-ray luminosity for GX 9+1. If the actual $N_{\rm H}$ toward GX 9+1 is indeed on the high end of the range considered, the positive slope of the NIR spectrum of GX 9+1 points at thermal emission. Given the uncertainties in the extinction law and $N_{\rm H}/A_V$ ratios, we refrain from trying to distinguish between viscous heating and heating by X-ray reprocessing. The positive slope is inconsistent with a dominant contribution from jet synchrotron emission in this wavelength region. In this respect, GX 9+1 is similar to the other two bright atolls and most Z sources that have been studied in the NIR, which also have NIR spectra with positive slopes. For GX 9+1 and the other bright atolls, there is no indication for the presence of a strong jet given that these sources have not been detected at radio wavelengths (Berendsen et al. 2000). This is not surprising as jets are commonly associated with NS-LMXBs that are in relatively hard X-ray spectral states. The bright atolls, on the contrary, are typically found in an X-ray–soft state. Therefore, we can also turn the argument around: the assumption that there is no jet in GX 9+1, implies that α must be positive. This can be used as another argument in favor for the higher $N_{\rm H}$ values toward the system.

[11] We caution that our FIRE spectra are not properly flux-calibrated, but have been corrected by a telluric standard; this should restore the approximate shape of the spectra if the difference in slit losses between the telluric standard and GX 9+1 does not introduce a color-dependent effect on the spectra.

If the thermal NIR emission is mainly coming from the outer disk, where X-ray heating dominates over viscous heating, there should be a connection between the K_s-band luminosity, the X-ray luminosity, and the orbital period (which sets the size of the disk). The existence of such a correlation has been demonstrated by Revnivtsev et al. (2012), analogously to the work by van Paradijs & McClintock (1994) for the case of the optical emission of X-ray binaries. We have used their empirical formula to constrain the orbital period of GX 9+1 based on its X-ray luminosity and estimated absolute K_s magnitude. We assume that ∼70% of the X-ray luminosity in the 0.12–18 keV band is emitted in the 2–10 keV band[12], for which Revnivtsev et al. derived their relation. The resulting range is not very restrictive: for $d = 4$ kpc and $N_{\rm H} = 8 \times 10^{21}\,{\rm cm}^{-2}$ we find $P_b \approx 1.0$ hr, whereas $d = 8.3$ kpc and $N_{\rm H} = 1.5 \times 10^{22}\,{\rm cm}^{-2}$ give $P_b \approx 4.0$ hr. Again, the choice of $N_{\rm H}/A_V$ ratio has a small ($\lesssim$5%) effect. Follow-up photometric monitoring of the NIR counterpart may reveal the actual orbital period of GX 9+1. The long-term variation in the X-ray light curve that is clearly visible in Figure 1 is unlikely to be related to the orbit but could reflect very-low frequency noise or solar-like magnetic-activity cycles (Durant et al. 2010; Kotze & Charles 2010)

The authors would like to thank J. Fridriksson, R. Remillard, P. Sullivan, and M. Matejek for obtaining part of the observations. We acknowledge the use of data products from VVV Survey observations made with the VISTA telescope at the ESO Paranal Observatory under program ID 179.B-2002.

Facilities: CXO, *RXTE*, MAXI, *Magellan*:Baade (PANIC, FourStar, FIRE), NTT (SOFI).

REFERENCES

Baglio, M. C., D'Avanzo, P., Campana, S., et al. 2016, A&A, 587, A102
Bandyopadhyay, R., Shahbaz, T., Charles, P. A., van Kerkwijk, M. H., & Naylor, T. 1997, MNRAS, 285, 718
Bandyopadhyay, R. M., Shahbaz, T., Charles, P. A., & Naylor, T. 1999, MNRAS, 306, 417
Berendsen, S. G. H., Fender, R., Kuulkers, E., Heise, J., & van der Klis, M. 2000, MNRAS, 318, 599
Bertin, E. 2006, in ASP Conf. Ser. 351, Astronomical Data Analysis Software and Systems XV, ed. C. Gabriel et al. (San Francisco, CA: ASP), 112
Bertin, E., Mellier, Y., Radovich, M., et al. 2002, in ASP Conf. Ser. 281, Astronomical Data Analysis Software and Systems XI, ed. D. A. Bohlender, D. Durand, & T. H. Handley (San Francisco, CA: ASP), 228
Bessell, M. S., & Brett, J. M. 1988, PASP, 100, 1134
Bochanski, J. J., Burgasser, A. J., Simcoe, R. A., & West, A. A. 2011, AJ, 142, 169
Callanan, P. J., Curran, P., Filippenko, A. V., et al. 2002, ApJL, 574, L143
Cardelli, J. A., Clayton, G. C., & Mathis, J. S. 1989, ApJ, 345, 245
Casares, J., Charles, P., & Kuulkers, E. 1998, ApJL, 493, L39
Chakrabarty, D., & Roche, P. 1997, ApJ, 489, 254
Corbet, R. H. D., Thorstensen, J. R., Charles, P. A., et al. 1986, MNRAS, 222, 15
Cornelisse, R., Casares, J., Charles, P. A., & Steeghs, D. 2013, MNRAS, 432, 1361
Cowley, A. P., Crampton, D., & Hutchings, J. B. 1979, ApJ, 231, 539
Curran, P. A., Chaty, S., & Zurita Heras, J. A. 2011, A&A, 533, A3
Drimmel, R., Cabrera-Lavers, A., & López-Corredoira, M. 2003, A&A, 409, 205
Durant, M., Cornelisse, R., Remillard, R., & Levine, A. 2010, MNRAS, 401, 355
Fender, R. P., & Hendry, M. A. 2000, MNRAS, 317, 1
Frank, J., King, A., & Raine, D. 1992, Accretion Power in Astrophysics (Cambridge: Cambridge Univ. Press)
Fridriksson, J. K. 2011, PhD thesis, Massachusetts Institute of Technology
Friedman, H., Byram, E. T., & Chubb, T. A. 1967, Sci, 156, 374
Gottlieb, E. W., Wright, E. L., & Liller, W. 1975, ApJL, 195, L33
Gottwald, M., Steinle, H., Pietsch, W., & Graser, U. 1991, A&As, 89, 367
Güver, T., & Özel, F. 2009, MNRAS, 400, 2050
Harrison, T. E., Gelino, D. M., Buxton, M., & Fost, T. 2014, AJ, 148, 22
Harrison, T. E., McNamara, B. J., Bornak, J., et al. 2011, ApJ, 736, 54
Hasinger, G., & van der Klis, M. 1989, A&A, 225, 79
Hertz, P., & Grindlay, J. E. 1984, ApJ, 282, 118
Hertz, P., & Wood, K. S. 1988, ApJ, 331, 764
Hinkle, K. H., Fekel, F. C., Joyce, R. R., et al. 2006, ApJ, 641, 479
Homan, J., Kaplan, D. L., van den Berg, M., & Young, A. J. 2009, ApJ, 692, 73
Homan, J., van der Klis, M., Fridriksson, J. K., et al. 2010, ApJ, 719, 201
Hynes, R. I. 2005, ApJ, 623, 1026
Iaria, R., Di Salvo, T., Burderi, L., et al. 2014, A&A, 561, A99
Iaria, R., di Salvo, T., Robba, N. R., et al. 2005, A&A, 439, 575
Jones, M. H., & Watson, M. G. 1989, in ESA Special Publication 296, Two Topics in X-Ray Astronomy, Vol. 1, ed. J. Hunt & B. Battrick (Paris: ESA), 439
Jonker, P. G., Fender, R. P., Hambly, N. C., & van der Klis, M. 2000, MNRAS, 315, L57
Kotze, M. M., & Charles, P. A. 2010, MNRAS, 402, L16
Kuulkers, E., van der Klis, M., Oosterbroek, T., et al. 1994, A&A, 289, 795
Levine, A. M., Bradt, H., Cui, W., et al. 1996, ApJL, 469, L33
Lin, D., Altamirano, D., Homan, J., et al. 2009a, ApJ, 699, 60
Lin, D., Remillard, R. A., & Homan, J. 2009b, ApJ, 696, 1257
Lucas, P. W., Hoare, M. G., Longmore, A., et al. 2008, MNRAS, 391, 136
Martini, P., Persson, S. E., Murphy, D. C., et al. 2004, Proc. SPIE, 5492, 1653
Matsuoka, M., Kawasaki, K., Ueno, S., et al. 2009, PASJ, 61, 999
Migliari, S., Tomsick, J. A., Miller-Jones, J. C. A., et al. 2010, ApJ, 710, 117
Minniti, D., Lucas, P. W., Emerson, J. P., et al. 2010, NewA, 15, 433
Monson, A., Persson, E., Murphy, D., Birk, C., & Kelson, D. 2011, FourStar Manual, http://instrumentation.obs.carnegiescience.edu/FourStar/Documents/FourStar_Documentation.pdf
Naylor, T., Charles, P. A., & Longmore, A. J. 1991, MNRAS, 252, 203
Nishiyama, S., Nagata, T., Tamura, M., et al. 2008, ApJ, 680, 1174
Nishiyama, S., Tamura, M., Hatano, H., et al. 2009, ApJ, 696, 1407
Ostlie, D., & Carroll, B. 2007, An Introduction to Modern Stellar Astrophysics (2nd ed.; San Francisco, CA: Benjamin Cummings Publishing Company)
Picaud, S., & Robin, A. C. 2004, A&A, 428, 891
Predehl, P., & Schmitt, J. H. M. M. 1995, A&A, 293, 889
Rayner, J. T., Cushing, M. C., & Vacca, W. D. 2009, ApJS, 185, 289
Revnivtsev, M. G., Zolotukhin, I. Y., & Meshcheryakov, A. V. 2012, MNRAS, 421, 2846
Russell, D. M., Fender, R. P., & Jonker, P. G. 2007, MNRAS, 379, 1108
Schultheis, M., Chen, B. Q., Jiang, B. W., et al. 2014, A&A, 566, A120
Shahbaz, T., Fender, R. P., Watson, C. A., & O'Brien, K. 2008, ApJ, 672, 510
Simcoe, R. A., Burgasser, A. J., Schechter, P. L., et al. 2013, PASP, 125, 270
Skrutskie, M. F., Cutri, R. M., Stiening, R., et al. 2006, AJ, 131, 1163
Taam, R. E. 1983, ApJ, 270, 694
Taylor, J. H., & Cordes, J. M. 1993, ApJ, 411, 674
Vacca, W. D., Cushing, M. C., & Rayner, J. T. 2003, PASP, 115, 389
Valencic, L. A., & Smith, R. K. 2015, ApJ, 809, 66
van den Berg, M., Grindlay, J., Laycock, S., et al. 2006, ApJL, 647, L135
van den Berg, M., Homan, J., Fridriksson, J. K., & Linares, M. 2014, ApJ, 793, 128
van Paradijs, J., & McClintock, J. E. 1994, A&A, 290, 133
Verbunt, F., & Zwaan, C. 1981, A&A, 100, L7
Wachter, S., & Margon, B. 1996, AJ, 112, 2684
Webbink, R. F., Rappaport, S., & Savonije, G. J. 1983, ApJ, 270, 678
White, N. E., Stella, L., & Parmar, A. N. 1988, ApJ, 324, 363

[12] Based on the best-fit model of Iaria et al. (2005).